Bioglass-fibre reinforced hydroxyapatite composites synthesized using spark plasma sintering for bone tissue engineering

Muhammad Rizwan[1,2,*], Ali Dad Chandio[1], Muhammad Sohail[3], M. Nasir Bashir[4], Sumra Yousuf[5,6], Rodianah Alias[2,7,*], Hammad ur Rehman[1], M. Hamdi[8], Wan Jeffrey Basirun[9]

[1]*Department of Metallurgical Engineering, Faculty of Chemical and Process Engineering, NED University of Engineering and Technology, 75270, Karachi, Pakistan*
[2]*Department of Mechanical Engineering, University of Malaya, 50603 Kuala Lumpur, Malaysia*
[3]*Department of Materials Engineering, Faculty of Chemical and Process Engineering, NED University of Engineering and Technology, 75270, Karachi, Pakistan*
[4]*National University of Sciences and Technology Islamabad, Pakistan*
[5]*Department of Building and Architectural Engineering, Faculty of Engineering & Technology, Bahauddin Zakariya University, 60000 Multan, Pakistan*
[6]*Department of Civil Engineering, University of Malaya, 50603 Kuala Lumpur, Malaysia*
[7]*Faculty of Innovative Design & Technology, University Sultan Zainal Abidin, 21030 Kuala Terengganu, Malaysia*
[8]*Chancellery office, University of Malaya, 50603 Kuala Lumpur, Malaysia*
[9]*Department of Chemistry, Faculty of Science, University of Malaya, 50603 Kuala Lumpur, Malaysia*

Abstract

Hydroxyapatite (HA) exhibits several desirable characteristics, but it still lacks osteoinduction, which is a necessary requirement for a bone scaffold. HA-based composites with different amounts of Bioglass® (BG) were prepared using spark plasma sintering (SPS). Careful selection of the SPS parameters avoided undesirable reactions between the calcium phosphate (CaP) and bioglass (BG present in the form of powder and fibres), as confirmed through X-ray diffraction analysis. Scanning electron microscopy images of the composite scaffolds revealed a fibre like appearance of the glassy region. The in vitro bioactivity and biodegradation analyses were performed by immersing the composites in simulated body fluid (SBF) and tris(hydroxymethyl)aminomethane (Tris), respectively. The ability to obtain only the CaP phase and glassy phase with desirable bioactive and biodegradation behaviour, indicated that these SPS scaffolds can be employed as bone scaffolds for clinical trials, after further in vivo analyses.

Keywords: hydroxyapatite, Bioglass®, spark plasma sintering, bioactivity, biodegradation

I. Introduction

Bone tissue regeneration has received huge research interest recently due to a large number of patients suffering from bone damage. Bone is a dynamic tissue that continuously resorbs and redevelops, hence, it has a high tendency towards regeneration [1]. Synthetic ceramic materials such as calcium phosphates (CaPs) with composition similar to the natural bone are considered the strongest candidate for bone regenerative treatments. Good bioactivity and biocompatibility of CaPs make them suitable candidates for bone regeneration strategies [2,3]. Among the CaPs, hydroxyapatite (HA) has been widely researched for orthopaedic applications due to its high resemblance with the mineral component of the natural bone, high biocompatibility and osteoconductivity [4]. Natural bone is a composite material consisting of almost 65% carbonated hydrox-

*Corresponding author: tel: +923351221508,
e-mail: *engr.rizwan@neduet.edu.pk* (M. Rizwan)
rodianahalias@unisza.edu.my (R. Alias)

yapatite (CHA) and 35% collagen [5,6]. However HA based scaffold materials primarily lack the mechanical strength, degradation rate, bioactivity response and osteointegration [7]. Moreover, HA does not exhibit the ability to stimulate primitive undifferentiated cells to develop bone-forming cells [8].

Efforts have been made to reinforce scaffolds with different types of fibres or nanoparticles to mimic the natural bone structure. A lot of work has been devoted to strengthen the bioceramics with carbon nanotubes (CNTs), graphene, graphene oxide and reduced graphene oxide [9]. The biocompatibility of these reinforcing materials is acceptable, but the long term exposure in the human body is not fully understood and it is the subject of considerable research nowadays [10]. Polymeric fibres like chitosan, silk, poly lactic acid (PLA) and poly caprolactone (PCL) have been also incorporated into these bioceramics [11]. These materials have excellent biocompatibility and are also bioresorbable, but due to a low thermal stability, the high temperature sintering of these bioceramics is not possible [5].

Bioactive glass is an interesting bioresorbable compound as the reinforcement material [12]. The biocompatibility of bioactive glasses is well established and they have been used as scaffold materials. The elemental composition of these glasses is quite similar to that of CaP based bioceramics. Bioactive glasses in different forms such as particles, granules, fibres or scaffolds have been employed for bone regeneration in past decade, due to their bone-bonding property and ability to stimulate the formation of new bone [13,14]. On the other hand Bioglass® (BG - 45 wt.% SiO_2, 24.5 wt.% Na_2O, 24.5 wt.% CaO and 6 wt.% P_2O_5) exhibits the highest bioactivity, improved osteointegration, ability to develop simultaneous bonds with hard and soft tissues, with additional features such as angiogenesis and antibacterial character. Researchers have attempted to develop composite scaffolds by combining HA and BG for improved overall performance with the desired characteristics, but it is still unsuccessful due to the devitrification process and excessive reaction between the two constituents [15–18]. Thus, there is a dire need to fabricate scaffold materials composed of BG and HA which are free from the excessive chemical reactions and devitrification process, which is expected to significantly improve the biological performance and control of the bioresorption rate [19].

In this study, composite scaffolds have been prepared by combining HA and BG (fibres and particles) through the spark plasma sintering (SPS) technique, to mimic the fibre (collagen) reinforced ceramic (HA) composite design of the natural bone. There are no previous reports of the reinforcement of bioglass fibres (BGF) in HA matrix using the SPS technique. BG particles (5 wt.%) were added to eliminate the undesirable $CaHPO_4$ phase present in the procured HA. The BG fibres (up to 20 wt.%) were added into the HA to prepare the BG fibre reinforced HA composite scaffolds. This is the first report on SPS of HA based scaffolds containing BG fibres and powders. The SPS is a unique sintering technique that offers simultaneous compaction and sintering with less severe compaction and sintering parameters compared to the conventional compaction and sintering techniques [20]. The SPS technique uses relatively lower compaction pressure (maximum 3.67 MPa in this study) and sintering temperature (1000 °C), which prevents the fracture of glass fibres and melting/crystallization of BG, respectively. Furthermore, the low SPS pressure facilitates the preparation of porous scaffolds.

II. Experimental

Hydroxyapatite-Bioglass® composites with different amount of Bioglass® in the form of fibres and powders were prepared. Submicron sized hydroxyapatite powder (Cod. 21223), that contained traces of $CaHPO_4$, was purchased from Sigma Aldrich, Malaysia. The fibres (with average diameter of 21.5 μm) and microspheres (with average size of 200 μm) of BG 45S5 were purchased from XL SciTech Inc, US. The HA and BG (particles and fibres) were mixed for 6 h using ZrO_2 balls in a polyethylene flask. The BG particles (5 wt.%) were added into the HA to avoid the undesirable $CaHPO_4$ phase formation, which was inherently present in the procured HA, as discussed in an earlier study [19]. The fibres containing premixes were prepared cautiously to prevent the clustering of the BG fibres. The de-clustering was carried out manually using tweezers. The addition of BG fibres was not feasible beyond 20 wt.%, due to the lower mobility of the powders and the inability of the powders to accommodate the fibres without clustering. The premixed compositions are given in Table 1.

Table 1. Sample composition

Sample	HA [wt.%]	BG [wt.%]	BGF [wt.%]
HA	100	-	-
HB5	95	5	-
HBF-5	90	5	5
HBF-10	85	5	10
HBF-15	80	5	15
HBF-20	75	5	20

2.1. Consolidation of powders

The premixed compositions and pristine HA were spark plasma sintered (SPS-1030S, SPS Syntex system) at extremely low pressure or the minimum allowed pressure in the SPS technique. For each SPS cycle, 8 g of premixed powder was filled in a ∅30 mm graphite die. The SPS process was carried out at 1000 °C and a heating rate of 50 °C/min with 30 min dwell. The compaction pressure was initially maintained at 1.83 MPa for a smooth passage of the current, which was raised to 3.67 MPa maximum pressure during the holding stage. Upon the completion of holding, the samples are
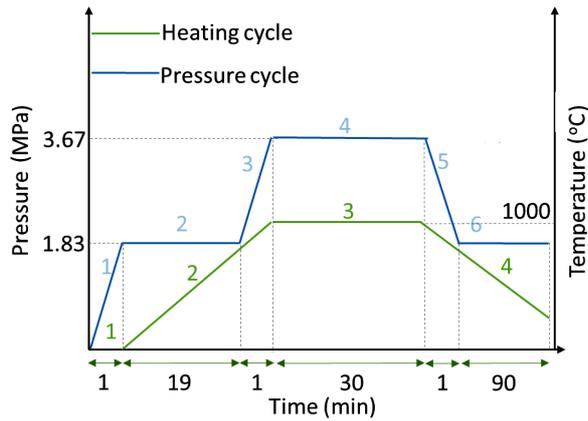
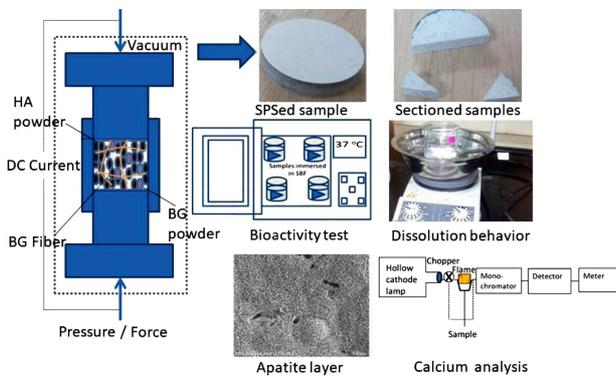**Figure 1. Heating and pressurizing cycle for SPS**

Figure 2. Schematic illustration of adopted methodology

allowed to cool to room temperature under the same load. Figure 1 explains the adopted sintering and compaction cycle.

2.2. Materials characterization

Further characterization of the SPS samples was carried out after cutting them by using a diamond saw. The characterization of phases was performed by powder X-ray diffraction (XRD) using Shimadzu XRD-6100 (Japan) diffractometer, with a Cu Kα (monochromated $\lambda = 1.54056$ Å) radiation at 30 mA and 40 kV. The scanning was performed at 2 °C/min with a step size of 0.02° in the 2θ range from 10° to 80°. The microstructure of the SPS samples was analysed after deposition of a thin Pt layer on the ground and polished samples, in order to minimize the charging effect. A Phenom Pro X table top scanning electron microscope (SEM) was employed to examine the microstructural features of the samples while field emission scanning electron microscope (FESEM, Hitachi SU 8220, Japan) was employed (after deposition of a thin Au layer on the samples) to observe the developed apatite layer. The EDAX analysis of the SPS samples and the apatite layer were performed using energy dispersive X-ray analyser attached to each electron microscope. A microhardness tester (Schimadzu HMV-G21 DT) was used to characterize the glassy regions while a Vickers macro-hardness tester (Wolpert Wilson 450 SVA) was used to characterize the

CaP phase. The hardness values are the average obtained from 10 indents.

2.3. In vitro bioactivity analysis

The growth of the apatite layer (resembling the natural bone) was analysed by evaluation of *in vitro* bioactivity of the SPS samples. The bioactivity analysis was performed by immersing the samples in simulated body fluid (SBF) as per protocol described by Kokubo and Takadama [21]. The chemical composition of SBF exhibits high resemblance to the human blood plasma [22]. The adopted procedure for complete bioactivity tests is explained in our earlier article [23]. The morphological characterization of the grown apatite layer was analysed using FESEM (after deposition of a thin Au layer), while its composition was determined using EDAX. The infrared transmittance behaviour of the grown apatite layer was confirmed using FTIR Spectrum 400 (Perkin Elmer, US).

2.4. In vitro biodegradation analysis

The resorption behaviour of the SPS composites was predicted on the basis of *in vitro* Ca dissolution behaviour of the pristine HA, BG and composites. The degradation behaviour of CaPs in biological environments must be predicted and optimized to accommodate the rate of new bone formation of the individual patient [23]. The concentration of Ca was determined using absorption spectroscopy (AAS Perkin Elmer A Analyst 400 AA Spectrometer, US) after carrying out a non-contact stirring for 5 h in Tris (pH = 7.4) at 37 °C. The preparation of the standard sample for the calibration of Ca content and the experimental biodegradation analysis was explained in our earlier report [24]. Figure 2 presents the schematic illustration of the adopted methodology. The synthesized and sectioned samples have been exposed at body temperature (i.e. 37 ± 1 °C) for bioactivity and dissolution analysis. In the next phase, the developed apatite layer is characterized by using FESEM and Ca content analysis using AAS.

III. Results and discussion

The SPS disk-shaped samples of 2-inch diameter, were physically stable and were easily drawn out of the graphite die. The surface did not show any signs/marks that could indicate the reaction between the samples and the graphite die. SPS is a pressure assisted sintering technique which densifies the samples using the creep mechanism. The final density of the SPS compacts is primarily driven by the sintering temperature and compaction pressure [37,38]. These driving parameters were programmed on the lower magnitude to control the porosity in the final compacts.

3.1. Phase analysis

Figure 3 presents XRD results of all the SPS samples. XRD analysis confirmed the unique ability of SPS technique and careful selection of its parameters to
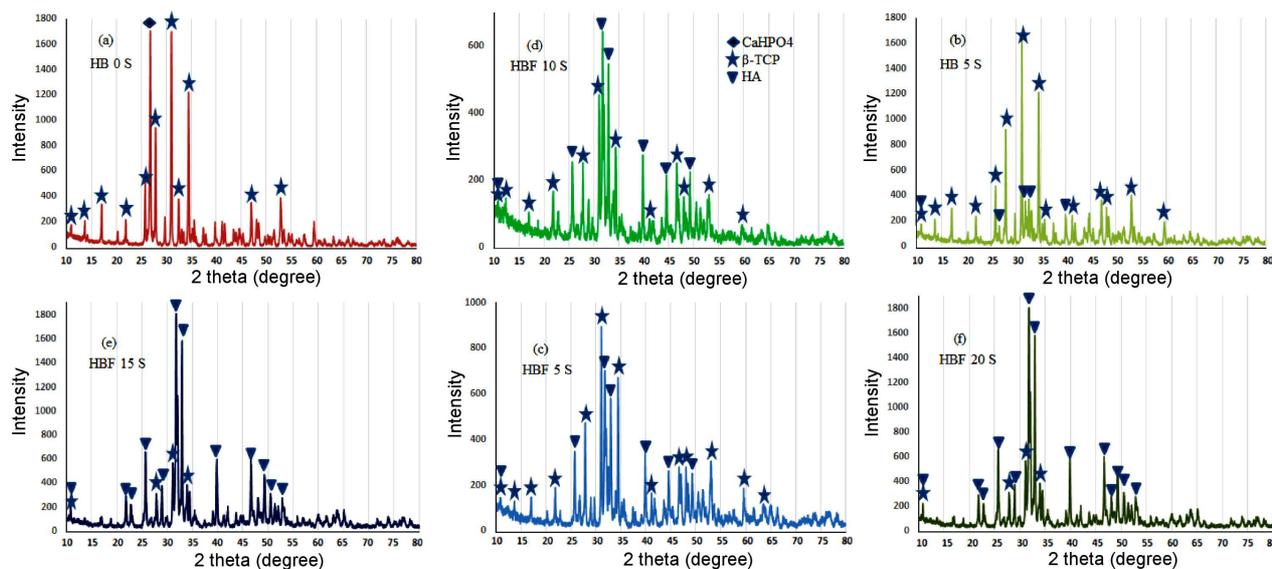
Figure 3. XRD patterns of prepared SPS compositions

avoid undesirable reactions between the HA and BG, as well as the crystallization of BG. The characteristic BG phases (such as $Na_2Ca_2SiO_6$ and $Na_2Ca[PO_4]_2SiO_4$) [25] are absent in the diffractograms, indicating the successful prevention of the BG crystallization. Furthermore, the phases indicative of the severe chemical reaction between the HA and BG, such as $Ca_5(PO_4)_2SiO_4$, $Na_2HPO_4 \cdot 7H_2O$, rhenanite and wollastonite as reported previously [15,26,27], are also absent. Desogus *et al.* [28] attempted to prepare HA-BG composites using SPS, however they also observed crystalline $Na_6Ca_3Si_6O_{18}$ phase formation from the reaction between HA and BG. In our study, all the composite samples only composed of CaP phases (HA and β-TCP) and a glassy content as evident from the diffractograms in Fig. 3. The HA used for this study inherently had traces of $CaHPO_4$. The presence of $CaHPO_4$ traces in the same HA (Code 21223 supplied by Sigma Aldrich) was confirmed by Cuccu *et al.* [29]. The increased tendency of the HA to transform into the β-TCP phase upon SPS (even at lower temperatures) was reported in the same study [29]. SPS performed for 30 min at 1000 °C completely transformed the HA into the β-TCP phase with traceable $CaHPO_4$ phase, as in Fig. 3b. With the addition of BG particles (5 wt.%), $CaHPO_4$ was totally eliminated with the formation of the single β-TCP phase.

The diffusion of Ca from the Ca-rich CaP phase to the BG phase, in addition to the diffusion of Si and Na from the BG phase to the CaP phase, was inevitable and primarily due to the ample sintering time which favoured this diffusion. This diffusion allows the stabilization of vitreous BG and the reprecipitation of HA into the β-TCP phase. The mechanisms involved in the reprecipitation of HA and stabilization of vitreous BG were explained in our earlier work [19]. The presence of BG powder and BGF enhances this diffusion which stabilizes the vitreous BG and reprecipitation of HA with in-

creased BG content. As a quantitative comparison, the ratio of HA/β-TCP was estimated from the peaks' intensities present in the reference files of β-TCP and HA. The matching reference file 96-101-1243 for HA shows the highest intensity for d-spacing = 2.812 Å; for the β-TCP 00-009-0169 reference file was used showing the highest diffracted intensity for d = 2.880 Å. The addition of BGF (0–20 wt.%) strengthened the HA intensity at the expense of the β-TCP phase leaving a negligible content of β-TCP in the composite scaffold HBF-20. The HA/β-TCP ratios for the HBF-10, HBF-15 and HBF-20 were 1.4977, 3.7118 and 4.2380, respectively.

3.2. Microstructural analysis

The microstructural analysis (Fig. 4) confirmed the presence of the glassy phase and porosity in the SPS samples containing the BGF. The increase in porosity with the increase in BG content was also reported in an earlier study [19]. The incorporation of BGF up to 20 wt.% yields a similar increase in the porosity due to the diffusion during SPS process in accordance with the study. The glassy region observed in these samples exhibited a fibre-like morphology, particularly for the samples containing BGF with 10 wt.% and more. As the fibres possess a higher aspect ratio, their morphology was sustained, suggesting that no melting had occurred during SPS process. The glassy regions with higher aspect ratio were observable at a relatively lower magnification. Thus, glassy regions are visible in Figure 4.

3.3. EDAX analysis and elemental mapping

The slight diffusion of Si and Na from the BGF phase to the CaP phase is evident from the EDAX analysis (Fig. 5). The concentration gradient between the BGF and CaP phase primarily drives the diffusion of these elements due to the presence of an electric field [30]. The penetration of Na and Si into the HA lattice as a result
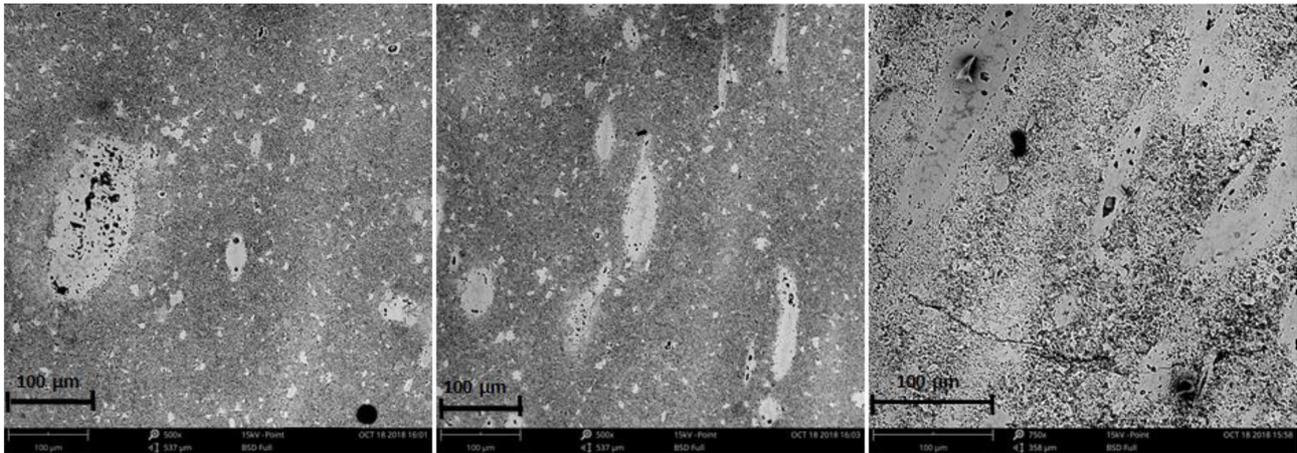
Figure 4. SEM analysis of HBF-5 (a), HBF-10 (b) and HBF-20 (c) showing elongated morphology of BGF in CaP matrix
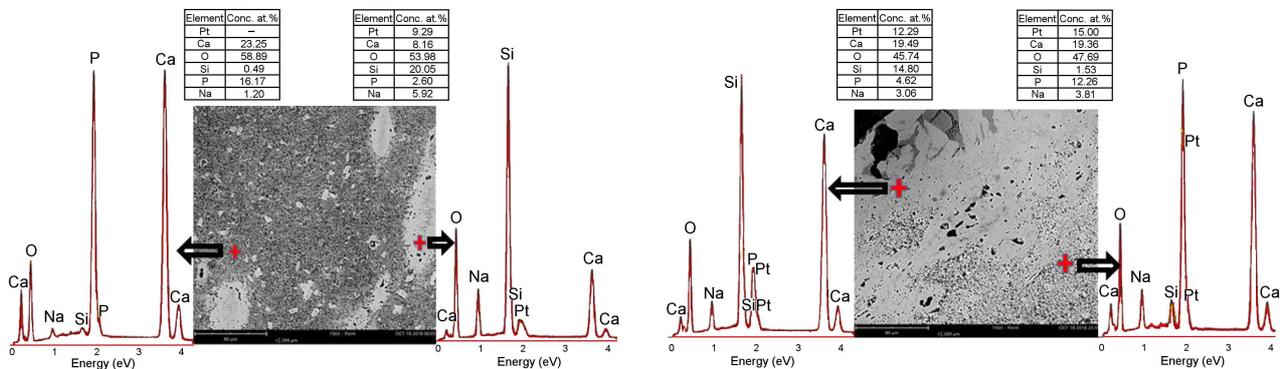

Figure 5. EDAX analysis of HBF-10 (a) and HBF-20 (b)

of diffusion, stabilizes it against the transformation into the β-TCP phase [31]. The diffused Na replaces the Ca while the diffused Si replaces the OH^- in the HA lattice which prevents the transformation [32]. This displacement of Ca from the HA lattice, and the inherent concentration gradient of Ca between the HA and BGF is the driving force for the penetration of Ca into the BGF. The replacement of Na in the BGF hinders the BG crystallization as observed by other researchers [28,33,34]. The glassy region is richer in Si and Na, while the CaP region still confirms the diffusion of Na and Si. The CaP phase in HBF-10 (Fig. 5a) shows higher Ca and P content with a trace concentration of Na and Si, while the glassy region exhibits a higher Si content, with a relatively lower amounts of Ca, Na and P. A similar pattern is visible for the HBF-20 sample (Fig. 5b).

The elemental distribution was also confirmed through the elemental mapping of the HBF-20 sample, as in Fig. 6. The top left glassy region is rich in Si (Fig. 6d) and Na (Fig. 6e). At the same time, the significant diffusion of Na and Si is clearly visible throughout the microstructure. This diffusion of Si and Na into the CaP region is attributed to the stabilization of the HA, as discussed earlier. The faster diffusion of Na at these sintering conditions is due to the relatively small size of Na and gives a higher contrast in the CaP and glassy regions. Similarly, the CaP region exhibits a stronger contrast of the Ca and P (Figs. 6b and 6c). The Ca and P

are inherently present in both BG and HA, hence their appearance is visible in the CaP and glassy regions, but an obvious darker contrast is present in the CaP regions.

3.4. Physicochemical characterization

Table 2 presents the physicochemical characteristics of the SPS samples. The bulk density of the composite samples decreases with the increase in the BGF content. Inherently, the BG possesses a lower density ($2.45\,\mathrm{g\,cm^{-3}}$) compared to HA ($3.156\,\mathrm{g\,cm^{-3}}$) [19,35]. The HA transformation into the β-TCP phase during SPS process yields the highest density owing to the expansive transformation. This expansive transformation is associated with the pore closure effect, resulting in an increased hardness of the sample. The relative phase content of HA increases significantly with the addition of BG and BGF, which resulted in a decreased bulk/relative density. The lower density of the composite samples consequently decreases the Vickers hardness index of the CaP phase. However, the volume of the glassy region is increased with the overall increase in the BG content (powder + fibres). The glassy region exhibited a higher hardness index compared to the CaP region. A microhardness indent on the glassy region of the HBF-10 sample is shown in Fig. 7a. Similarly, in Fig. 7b the downward trend of the bulk density (with increased BG content) is plotted for the composite samples.
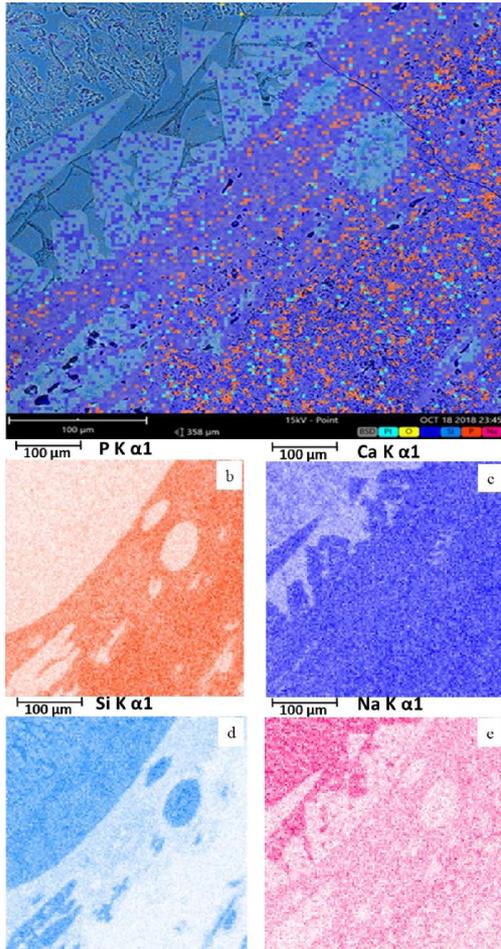
Figure 6. Schematic illustration of adopted methodology

The pristine BG underwent SPS under similar processing conditions to investigate the Ca dissolution behaviour (an estimation of biodegradation rate), which yields a dense (~98 %TD) disk with a much higher Ca dissolution compared to the pure HA (~92 %TD). The Ca dissolution rate of the BG (control) and all SPS samples are plotted graphically in Fig. 7b. The HBF SPS samples exhibit enhanced Ca dissolution rate with increased BGF content. The dissolution rate of the HBF-10 is significantly higher than the HBF-5 due to the increased BG content, but the curve slope eventually becomes very low with further increase in the BGF content. This slow increase may be attributed to the relatively high content of HA in the HBF-15 and HBF-20 samples, as the dissolution rate for HA is much lower than for the β-TCP phase [36]. The increased HA content in the samples somewhat counterbalances the increased dissolution of Ca with increased BG content.

3.5. In vitro bioactivity behaviour

The *in vitro* characterization of biomaterials via immersion in SBF represents the behaviour of the biomaterials in real physiological environments in the human body. The ability of the biomaterials to bond with human hard tissues in the physiological environment is associated with their tendency to develop a carbonated apatite (bone-like apatite) layer in the SBF [37,38]. The SPS HBF scaffolds formed a biomimetic hydroxyapatite layer on the surface as shown for the HBF-10 sample at different magnifications in Fig. 8, when immersed in SBF for 7 days. The formed apatite layer exhibited a typical morphology (porous bone-like apatite

Table 2. Physicochemical characteristics of all the SPS samples

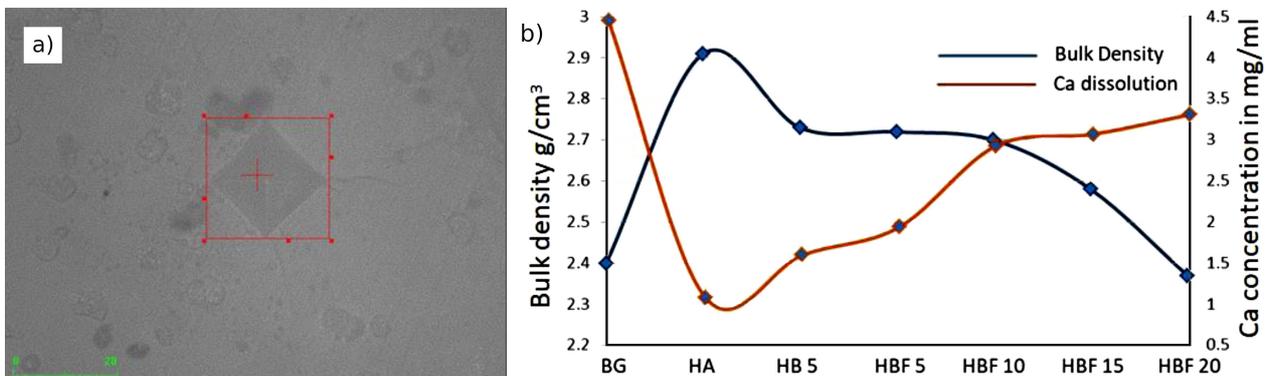| Sample code	Bulk density [g cm^{-3}]	Relative density [%TD]	Average HV2 hardness	Average HV2 micro-hardness of glassy region	Final concentration of Ca [mg/ml]
BG	2.4	98		462	4.45
HA	2.91	92.2	183.30	–	1.08
HB5	2.73	88.6	29.30	–	1.60
HBF5	2.72	88.85	39.95	427	1.94
HBF10	2.70	89.40	45.7	390	2.93
HBF15	2.58	86.72	51.35	414	3.07
HBF20	2.37	80.70	56.22	474	3.31

Figure 7. Micrograph of the microhardness indent on the BGF phase of HBF-10 (a) and graphical representation of the bulk density and Ca dissolution behaviour of all SPS samples (b)
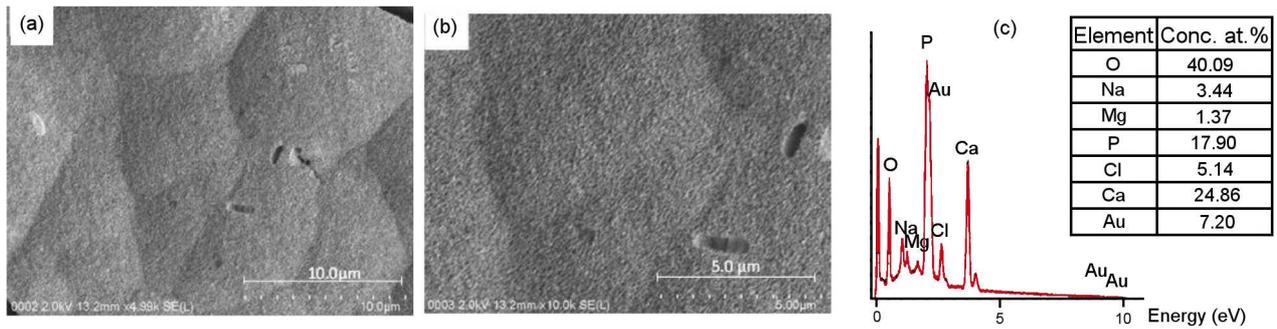
Figure 8. Apatite layer formation on SPS HBF 10 when immersed for 7 days in SBF - SEM images (a,b) and EDAX (c)
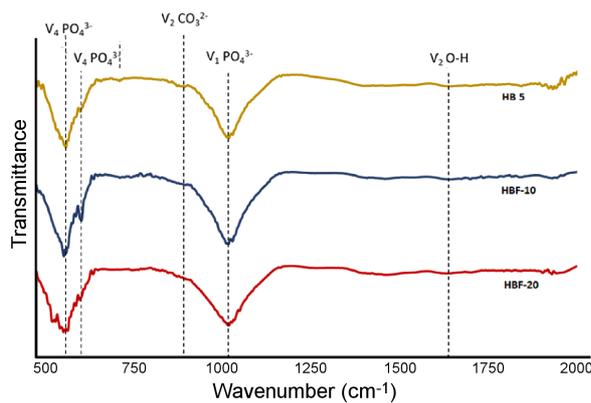

Figure 9. FTIR analysis of HBF samples

with drying cracks), in accordance with the morphology reported by Miller *et al.* [39]. Relatively large pores present on the apatite layer (in Fig. 8b) are due to water evaporation during the drying process [40]. The EDAX analysis (Fig. 8c) confirms the composition of the apatite layer. The presence of Ca and P with a trace content of Mg, Na and Cl could be due to the deposition from the SBF solution, in addition to apatite layer formation. A similar observation was also reported by Padilla *et al.* [41].

The FTIR analysis was used to confirm the presence of the different functional groups in the phases. The infrared transmittance behaviour of the developed apatite layers resembles the characteristic pattern of the biomimetic HA [42], as shown in Fig. 9. The characteristic bending for v_4 PO_4^{3-} is visible around 550 and $600\,cm^{-1}$. The C–O vibration which confirms the presence of the carbonated HA is observed around $870\,cm^{-1}$. Similarly, the characteristic bending vibration of v_3 PO_4^{3-} is observed at $1050\,cm^{-1}$ while the O–H vibration occurs at $1630\,cm^{-1}$.

IV. Conclusions

The careful selection of SPS control parameters afforded the synthesis of BG (fibres and powders) reinforced HA based composite scaffolds comprising of the glassy phase and CaP phase only. The BGF retained their shape factor characteristic of the high aspect ratio fibres. The unique ability of SPS to synthesize com-

posite scaffolds with BGF helps to mimic the natural bone's architecture by using HA and BG. The XRD analysis confirmed the presence of the pure CaPs along with the glassy phase. The HA/β-TCP ratio increased proportionally with an overall increase in the BG content, and the highest ratio (i.e. 4.2380) was observed in the HBF-20 sample. The scaffolds exhibited a Vickers hardness index (CaP phase) comparable to the natural bone, in addition to maintaining the bone's architecture. Moreover, the *in vitro* bioactivity analysis confirmed the ability of the biomimetic apatite formation. Similarly, desirable biodegradation behaviour (a necessary feature for bone remodelling) was observed using the *in vitro* Ca dissolution analysis. The Ca dissolution increased significantly with an overall increase in the BG content. The HBF-20 exhibited the highest Ca dissolution among all composite samples. From the above findings, the BGF reinforced HA composites are attractive materials for bone scaffolding applications. However, further mechanical characteristics (toughness and compressive strength) are needed before these scaffolds can be employed for *in vivo* analysis, prior to clinical trials.

References

1. H. Qu, H. Fu, Z. Han, Y. Sun, "Biomaterials for bone tissue engineering scaffolds: A review", *RSC Adv.*, **9** [45] (2019) 26252–26262.
2. S.V. Dorozhkin, "Calcium orthophosphate-based bioceramics and its clinical applications", pp. 123–226 in *Clinical Applications of Biomaterials: State-of-the-Art Progress, Trends, and Novel Approaches*. Ed. G. Kaur, Springer International Publishing: Cham, 2017.
3. M. Canillas, P. Pena, H. Antonio, M.A. Rodríguez, "Calcium phosphates for biomedical applications", *Bol. Soc. Esp. Cerám. Vidrio*, **56** [3] (2017) 91–112.
4. S. Khoshsima, A.Z. Alshemary, A. Tezcaner, S. Surdem, Z. Evis, "Impact of B_2O_3 and La_2O_3 addition on structural, mechanical and biological properties of hydroxyapatite",

Process. Appl. Ceram., 12 [2] (2018) 143–152.

5. Q. Fu, E. Saiz, M.N. Rahaman, A.P. Tomsia, "Toward strong and tough glass and ceramic scaffolds for bone repair", *Adv. Funct. Mater.*, **23** [44] (2013) 5461–5476.

6. M. Vallet-Regi, J.M. González-Calbet, "Calcium phosphates as substitution of bone tissues", *Prog. Solid State Chem.*, **32** [1-2] (2004) 1–31.

7. D. Bellucci, S. Braccini, F. Chiellini, P. Balasubramanian, A.R. Boccaccini, V. Cannillo, "Bioactive glasses and glass-ceramics versus hydroxyapatite: Comparison of angiogenic potential and biological responsiveness", *J. Biomed. Mater. Res. Part A*, **107** [12] (2019) 2601–2609.

8. J. Huang, S. Best, R. Brooks, N. Rushton, W. Bonfield, "In vitro evaluation of nanosized carbonate-substituted hydroxyapatite and its polyhydroxyethylmethacrylate nanocomposite", *J. Biomed. Mater. Res. Part A*, **87** [3] (2008) 598–607.

9. H.A. Siddiqui, K.L. Pickering, M.R. Mucalo, "A review on the use of hydroxyapatite-carbonaceous structure composites in bone replacement materials for strengthening purposes", *Materials*, **11** [10] (2018) 1813.

10. S. Toyokuni, "Genotoxicity and carcinogenicity risk of carbon nanotubes", *Adv. Drug Delivery Rev.*, **65** [15] (2013) 2098–2110.

11. M.E. Frohbergh, A. Katsman, G.P. Botta, P. LAzarovici, C.L. Schauer, U.G.K. Wegst, P. Lelkes, "Electrospun hydroxyapatite-containing chitosan nanofibers crosslinked with genipin for bone tissue engineering", *Biomaterials*, **33** [36] (2012) 9167–9178.

12. O. Parkhomey, N. Pinchuk, O. Sych, T. Tomila, O. Kuda, H. Tovstonoh, V. Gorban, V. Kolesnichenko, Y. Evych, "Effect of particle size of starting materials on the structure and properties of biogenic hydroxyapatite/glass composites", *Process. Appl. Ceram.*, **10** [1] (2016) 1–8.

13. S. Zhao, J. Zhang, M. Zhu, Y, Zhang, Z. Liu, C. Tao, Y. Zhu, C. Zhang, "Three-dimensional printed strontium-containing mesoporous bioactive glass scaffolds for repairing rat critical-sized calvarial defects", *Acta Biomater.*, **12** (2015) 270–280.

14. D.S. Seo, J.K. Lee, "Dissolution-resistance of glass-added hydroxyapatite composites", *Metals Mater. Int.*, **15** [2] (2009) 265.

15. H. Demirkiran, A. Mohandas, M. Dohi, A. Fuentes, K. Nguyen, P. Aswath, "Bioactivity and mineralization of hydroxyapatite with bioglass as sintering aid and bioceramics with $Na_3Ca_6(PO_4)_5$ and $Ca_5(PO_4)_2SiO_4$ in a silicate matrix", *Mater. Sci. Eng. C*, **30** [2] (2010) 263–272.

16. H. Demirkiran, Y. Hu, L. Zuin, N. Appathurai, P.B. Aswath, "XANES analysis of calcium and sodium phosphates and silicates and hydroxyapatite-Bioglass® 45S5 co-sintered bioceramics", *Mater. Sci. Eng. C*, **31** [2] (2011) 134–143.

17. D. Bellucci, V. Cannillo, A. Sola, "A new highly bioactive composite for bone tissue repair", *Int. J. Appl. Ceram. Technol.*, **9** [3] (2012) 455–467.

18. D. Bellucci, A. Sola, M. Gazzarri, F. Chiellini, V. Cannillo, "A new hydroxyapatite-based biocomposite for bone replacement", *Mater. Sci. Eng. C*, **33** [3] (2013) 1091–1101.

19. M. Rizwan, M. Hamdi, W.J. Basirun, K. Kondoh, J. Umeda, "Low pressure spark plasma sintered hydroxyapatite and Bioglass® composite scaffolds for bone tissue repair", *Ceram. Int.*, **44** [18] (2018) 23052–23062.

20. Y.-H. Han, R. Gao, I. Bajpai, B.-N. Kim H. Yoshida A. Ni-eto, H.-W. Son, J. Yun, B.-K. Jang, S. JhungZ. Jingming, K.-H. Hwang, F. Chen, J.F. Shackelford, S. Kim, "Spark plasma sintered bioceramics – from transparent hydroxyapatite to graphene nanocomposites: A review", *Adv. Appl. Ceram.*, **119** [2] (2020) 57–74.

21. T. Kokubo, H. Takadama, "How useful is SBF in predicting in vivo bone bioactivity?", *Biomaterials*, **27** [15] (2006) 2907–2915.

22. V. Badisha, S. Shaik, R. Dumpala, B.R. Sunil, "Developing Mg-Zn surface alloy by friction surface alloying: In vitro degradation studies in simulated body fluids", *Int. J. Miner. Metall. Mater.*, **27** [7] (2020) 962–969.

23. M. Rizwan, K. Genasan, M.R. Murali, H.R.B. Raghavendran, R. Alias, Y.Y. Cheok, W.F. Wong, A. Mansor, M. Hamdi W.J. Basirun, T. Kamarul, "In vitro evaluation of novel low-pressure spark plasma sintered HA-BG composite scaffolds for bone tissue engineering", *RSC Adv.*, **10** [40] (2020) 23813–23828.

24. M. Rizwan, S. Yousuf, M. Sohail, M. Bashir, R. Alias, M. Hamdi, W. Basirun, "Synthesis, characterization, and in vitro biochemical analysis of hydroxyapatite-Bioglass® composite scaffolds for bone tissue repair", *JOM*, **72** [10] (2020) 3683–3692.

25. L. Lefebvre, J. Chevalier, L. Gremillard, R.Zenati, G. Thollel, D. Bernache-Assolant, A. Govin, "Structural transformations of bioactive glass 45S5 with thermal treatments", *Acta Mater.*, **55** [10] (2007) 3305–3313.

26. G. Goller, H. Demirkıran, F.N.Oktar, E. Demirkesen, "Processing and characterization of bioglass reinforced hydroxyapatite composites", *Ceram. Int.*, **29** [6] (2003) 721–724.

27. B. Devis, S. Antonella, C. Valeria, "Low temperature sintering of innovative bioactive glasses", *J. Am. Ceram. Soc.*, **95** [4] (2012) 1313–1319.

28. L. Desogus, A. Cuccu, S. Montinaro, R. Orru, G. Cao, D. Bellucci, A, Sola, V. Cannillo, "Classical Bioglass® and innovative CaO-rich bioglass powders processed by Spark Plasma Sintering: A comparative study", *J. Eur. Ceram. Soc.*, **35** [15] (2015) 4277–4285.

29. A. Cuccu, S. Montinaro, R. Orru, G. Cao, D. Bellucci, A, Sola, V. Cannillo, "Consolidation of different hydroxyapatite powders by SPS: Optimization of the sintering conditions and characterization of the obtained bulk products", *Ceram. Int.*, **41** [1] (2015) 725–736.

30. W.J. Wright, D.R. Askeland, *The Science and Engineering of Materials*, Nelson Engineering, 2015, p. 923.

31. J. Knowles, "Development of hydroxyapatite with enhanced mechanical properties: Effect of high glass additions on mechanical properties and phase stability of sintered hydroxyapatite", *British Ceram. Trans.*, **93** [3] (1994) 100–103.

32. M. Šupová, "Substituted hydroxyapatites for biomedical applications: A review", *Ceram. Int.*, **41** [8] (2015) 9203–9231.

33. M. Lockyer, D. Holland, R. Dupree, "NMR investigation of the structure of some bioactive and related glasses", *J. Non-Crystal. Solids*, **188** [3] (1995) 207–219.

34. D. Bellucci, V. Cannillo, A. Sola, "Calcium and potassium addition to facilitate the sintering of bioactive glasses", *Mater. Lett.*, **65** [12] (2011) 1825–1827.

35. M. Rizwan, M. Hamdi, W. Basirun, "Bioglass® 45S5-based composites for bone tissue engineering and functional applications", *J. Biomed. Mater. Res. Part A*, **105**

[11] (2017) 3197–3223.

36. S. Samavedi, A.R. Whittington, A.S. Goldstein, "Calcium phosphate ceramics in bone tissue engineering: a review of properties and their influence on cell behaviour", *Acta Biomater.*, **9** [9] (2013) 8037–8045.

37. C. Drouet, "Apatite formation: why it may not work as planned, and how to conclusively identify apatite compounds", *Biomed. Res. Int.*, **2013** (2013) 1–12.

38. K. Rezwan, Q. Chen, J. Blaker, A.R. Boccaccini, "Biodegradable and bioactive porous polymer/inorganic composite scaffolds for bone tissue engineering", *Biomaterials*, **27** [18] (2006) 3413–3431.

39. C. Miller, T. Kokubo, I. Reaney, P. Hatton, P. James, "Formation of apatite layers on modified canasite glass-ceramics in simulated body fluid", *J. Biomed. Mater. Res.*, **59** [3] (2002) 473–480.

40. P. Habibovic, F. Barrere, C.A. Blitterswijk, K. Groot, P. Layrolle, "Biomimetic hydroxyapatite coating on metal implants", *J. Am. Ceram. Soc.*, **85** [3] (2002) 517–522.

41. S. Padilla, J. Román, S. Sánchez-Salcedo, M. Vallet-Regi, "Hydroxyapatite/SiO_2-CaO-P_2O_5 glass materials: In vitro bioactivity and biocompatibility", *Acta Biomater.*, **2** [3] (2006) 331–342.

42. I.V. Pylypchuk, A. Petranovskaya, P. Gorbyk, A. Korduban, P. Markovsky, O. Ivasishin, "Biomimetic hydroxyapatite growth on functionalized surfaces of Ti-6Al-4V and Ti-Zr-Nb alloys", *Nanoscale Res. Lett.*, **10** [1] (2015) 338.